crystals

MDPI

Article

Growth and Characterization of All-Inorganic Halide Perovskite $CsPbF_3$ Single Crystals

Xinlong Yan [1], Kan Zhang [2,*], Chan Guo [1], Yi Lu [2], Kuiyao Du [1], Chen Peng [1], Xiaodie Hu [1], Yuzhen Jia [1], Bai Xu [1], Ruichen Wang [1], Weiheng Duan [1], Hetong Han [2], Zhaohui Song [2], Shiguo Liu [1] and Fan Yang [1,3,*]

[1] The Key Laboratory of Weak Light Nonlinear Photonics, School of Physics, Nankai University, Tianjin 300071, China
[2] The State Key Laboratory of Intense Pulsed Radiation Simulation and Effect, Northwest Institute of Nuclear Technology, Xi'an 710024, China
[3] Shenzhen Research Institute, Nankai University, Shenzhen 518083, China
* Correspondence: zhangkan8414@163.com (K.Z.); fan@nankai.edu.cn (F.Y.)

Abstract: Lead-based halide perovskite semiconductors have demonstrated considerable potential in optoelectronic applications. However, the lack of high-quality crystals suitable for research has led to rare reports on $CsPbF_3$ single crystals. Good quality $CsPbF_3$ single crystals were successfully grown using the Bridgman method. The structure, luminescence, and electrical properties of crystals were investigated. At room temperature, the crystal structure was determined to be cubic perovskite, with a calculated bandgap of 3.68 eV. The measured emission spectrum showed one broad emission peak at approximately 400 nm. Three decay time constants were obtained from a sum of exponential functions fit to the fluorescence decay curve: 0.4 ns, 2.4 ns, and 15.0 ns for fast, middle, and slow decay times, respectively. The decay times excited by pulsed X-ray were measured to be 2.2 ns and 10.2 ns, indicating that $CsPbF_3$ is an ultrafast scintillator. Furthermore, the electrical properties demonstrated that $CsPbF_3$ exhibits high ion mobility, which is approximately 20 times that of electron mobility.

Keywords: $CsPbF_3$; Bridgman method; semiconductor; ultrafast scintillation; ionic mobility

check for updates

Citation: Yan, X.; Zhang, K.; Guo, C.; Lu, Y.; Du, K.; Peng, C.; Hu, X.; Jia, Y.; Xu, B.; Wang, R.; et al. Growth and Characterization of All-Inorganic Halide Perovskite $CsPbF_3$ Single Crystals. *Crystals* **2023**, *13*, 765. https://doi.org/10.3390/cryst13050765

Academic Editor: Ludmila Isaenko

Received: 4 April 2023
Revised: 25 April 2023
Accepted: 27 April 2023
Published: 4 May 2023

Copyright: © 2023 by the authors. Licensee MDPI, Basel, Switzerland. This article is an open access article distributed under the terms and conditions of the Creative Commons Attribution (CC BY) license (https://creativecommons.org/licenses/by/4.0/).

1. Introduction

Lead-based halide perovskites with a stoichiometric ratio of ABX_3 (where A = MA^+, GA^+, and Cs^+; B = Pb^{2+}; X = Cl^-, Br^-, and I^-) exhibit high carrier mobility, long diffusion length, adjustable bandgap, and defect tolerance. Therefore, they are exceptional candidates for various applications such as photodetectors, radiation detectors, solar cells, light-emitting diodes, and other fields [1–7]. Compared with the organic-inorganic hybrid perovskites, all-inorganic perovskite $CsPbX_3$ (X = Cl^-, Br^-, and I^-) is more appealing for radiation detection due to its superior stability, optoelectronic performances, and radiation hardness. $CsPbI_3$ has garnered considerable attention due to its exceptional thermal stability and ideal bandgap of approximately 1.75 eV, making it an attractive candidate for tandem applications. Tan et al. showed a study on the thermal stability of low-dimensional perovskites that utilize hydrophobic organic ammonium salts and their potential to safeguard $CsPbI_3$ through passivation. The highest-performing solar cell device employing $CsPbI_3$ as its primary material demonstrated an unprecedented efficiency of 21.0% while sustaining high stability [8,9]. $CsPbBr_3$ quantum dots emit light at a narrow band at room temperature, which makes them highly desirable for use in conventional light-emitting devices as well as emerging quantum light sources [10]. He et al. reported that all inorganic perovskite $CsPbBr_3$ devices resolve ^{137}Cs 662 keV γ-rays with 1.4% energy resolution, the $CsPbBr_3$ detector exhibited an excellent hole mobility lifetime product of 8×10^{-3} cm^2 V^{-1}, and a long hole lifetime of up to 296 μs. This research has established perovskite $CsPbBr_3$ semiconductors as exceptional candidates for high energy γ-ray detection in the new generation [11]. Although $CsPbCl_3$ has received less

attention than $CsPbBr_3$, some researchers have reported its optical and photodetection properties. $CsPbCl_3$ crystals have shown excellent ultrafast scintillation at low-temperature and semiconductor detection performance [12,13].

In particular, aluminium gallium nitride ($Al_xGa_{1-x}N$) is used to fabricate the visible-blind photodetector where the band gap energy can be adjusted from 3.4 eV (GaN) to 6.2 eV (AlN) by modifying the composition parameter x. Typically, the composition is altered to achieve a long wavelength cut-off below 300 nm by selecting a sufficiently high value for x. Conventional photodiodes and Schottky barrier detectors can be created, although the latter are somewhat simpler to manufacture. Silicon carbide (SiC) photodiodes are sensitive to light with wavelengths below approximately 355 nm, making them suitable for visible-blind detection. $CsPbF_3$ perovskite semiconductors possess a relatively large band gap energy of approximately 3.68 eV and a direct band gap, resulting in a well-defined long wavelength cut-off. Compared to the difficulty of growing GaN and SiC crystals, $CsPbF_3$ single crystals are easier to obtain in excellent quality, indicating their potential for application in visible-blind photodetectors. $CsPbF_3$ is a direct bandgap semiconductor with optical activity, which can effectively be used in optical and optoelectronic devices [14]. Bouznik et al. investigated the fast conduction of fluoride ions in $CsPbF_3$ polycrystals using continuous wave and pulse NMR techniques. The $CsPbF_3$ crystals were grown from the melt in an Ar-HF mixture atmosphere using a high-frequency crystallization apparatus [15]. Berastegui et al. observed a transition of $CsPbF_3$ from a rhombohedral distorted perovskite structure to a cubic perovskite structure at 187 K through neutron diffraction experiments, and the transition was found to be discontinuous [16]. In the low-temperature phase, cations exhibit a parallel displacement away from the center of their anion polyhedrons, which proves the existence of ferroelectric properties [17]. The $CsPbF_3$ polycrystalline sample was prepared by mixing stoichiometric amounts of CsF and PbF_2 in a dry box filled with nitrogen gas. Wang et al. circumvent the multiple bottlenecks of Li^+ ion batteries by using $CsPbF_3$ as a solid-state electrolyte. The battery cycled stably at 25 °C for 4581 h without considerable capacity fade [18]. Therefore, this ternary compound exhibits potential characteristics in terms of its performance. The optical performance of $CsPbF_3$ has not been investigated and presented yet, mainly due to the difficulty in obtaining high-quality $CsPbF_3$ crystals. Most perovskite devices are based on polycrystalline and thin films, which are greatly affected by a high density of traps and grain boundaries. In contrast, single crystals have significantly lower trap densities. However, there is insufficient research on the optical performance of $CsPbF_3$ single crystals, and many blanks need to be filled. As a result, the potential application of polycrystalline devices is significantly limited.

In this study, good-quality $CsPbF_3$ single crystals were grown by the Bridgman method. The optical and luminescence properties of the crystal were characterized and analyzed. The results demonstrate that $CsPbF_3$ crystal exhibits ultrafast scintillation and has potential as an ultrafast scintillation crystal. Additionally, the electrical properties of the crystals were characterized, revealing that $CsPbF_3$ single crystals exhibit high ion mobility and can be applied as a semiconductor.

2. Materials and Methods

2.1. Crystal Growth of $CsPbF_3$

The Bridgman method involves using a furnace with a hot and cold zone to create a temperature gradient, where the hot zone is maintained at a temperature above the melting point of the crystal [19–21]. The melt moves from the hot zone to the cold zone to complete the crystallization of the material by controlling the descending system. This method is commonly used to prepare single crystals of alkali metal, alkaline earth metal halides, and fluorides. The $CsPbF_3$ single crystals were prepared using the vertical Bridgman method. The advantages of preparing $CsPbF_3$ single crystals by the Bridgeman method mainly include the following aspects. Firstly, the raw material is sealed in the crucible, which reduces the leakage and pollution caused by the volatilization of the raw material, so the

composition of the crystal is easy to control. Secondly, the perovskite structure can easily accommodate impurity atoms, which is conducive to the removal of volatile impurities, thereby improving the crystal quality. The experimental configuration for crystal growth is depicted in Figure 1. High-purity powders of CsF (99.99%, Aladdin) and PbF_2 (99.99%, Aladdin) were mixed in a 1:1 ratio and ground thoroughly. The raw materials were mixed and put into a platinum crucible. The crucible was then placed inside a sealed quartz crucible. The crucible was moved to the Bridgman furnace for the growth of single crystals. The furnace temperature was set to 30°C higher than the melting point of the growth crystal. After the raw material was melted and soaked for 24 h, the drop controller system started to work, and the growth rate was set to 0.5 mm/h. Subsequently, $CsPbF_3$ single crystal growth was started, and the temperature gradient in the solid-liquid interface was about 20–30 °C/cm. After the entire solution was crystallized, the furnace was cooled down to room temperature at a rate of 50 °C/h. The crystal boules obtained were cut into plates, polished, and sealed.

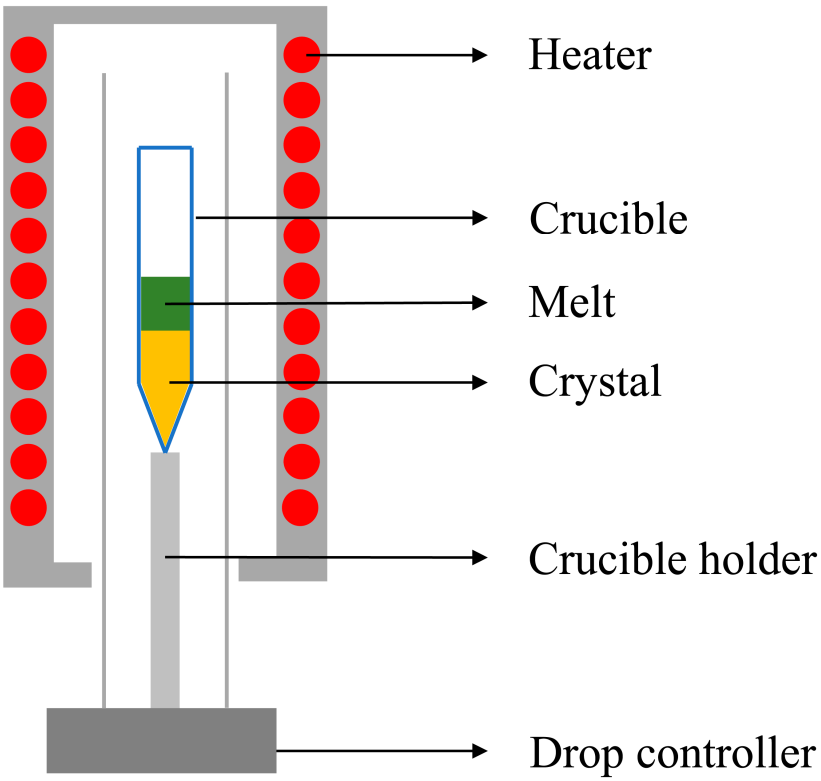

Figure 1. Schematic illustration of the crystal growth using the vertical Bridgman method.

2.2. Characterization

The crystal structure of $CsPbF_3$ was analyzed using a Bruker D8 advanced X-ray powder diffractometer with Cu Ka radiation (λ = 1.5406 Å), scanning 2θ from 10–90° with a step size of 0.02°. The thermal stability was tested using a NETZSCH STA449F3 instrument under a nitrogen atmosphere, with a heating program from 20 °C to 800 °C at a heating rate of 10 °C/min. The cathodoluminescence (CL) spectroscopy was tested using a HORIBA i-CLUE spectrometer with an electron beam voltage of 30 keV. The transmission spectrum was measured using a Hitachi U-4100 UV-vis spectrophotometer. The photoluminescence (PL) spectrum and fluorescence decay curve were measured using the FS5 spectrometer from Edinburgh, UK. The X-ray excited luminescence (XEL) and decay kinetic curve excited by X-rays were characterized with the Dongyi DF-7000X X-ray spectrometer with a rhodium target X-ray tube operating at 40 kV. Electrical properties were measured using the Keysight B1500A semiconductor analyzer.

3. Results and Discussion

3.1. Crystal Structure and Growth

Figure 2a illustrates the linear attenuation coefficients as a function of photon energy for several fast scintillation crystals, which were calculated using the NIST XCOM photon cross-section database. The red line in Figure 2a depicts the linear attenuation coefficient of $CsPbF_3$. It has been observed that the value of the red line is marginally higher than that of the other curves, indicating that a thinner layer of material is required to achieve effective photon cut-off. Compared with other ultrafast inorganic scintillators, $CsPbF_3$ has superior photon cut-off capabilities due to its high average atomic number (Cs: 55, Pb: 82, and F: 9) and relatively high density (ρ = 5.6 g/cm^3). The statement suggests that $CsPbF_3$ is capable of absorbing X-rays more efficiently compared to other materials, indicating its potential superiority in X-ray imaging applications.

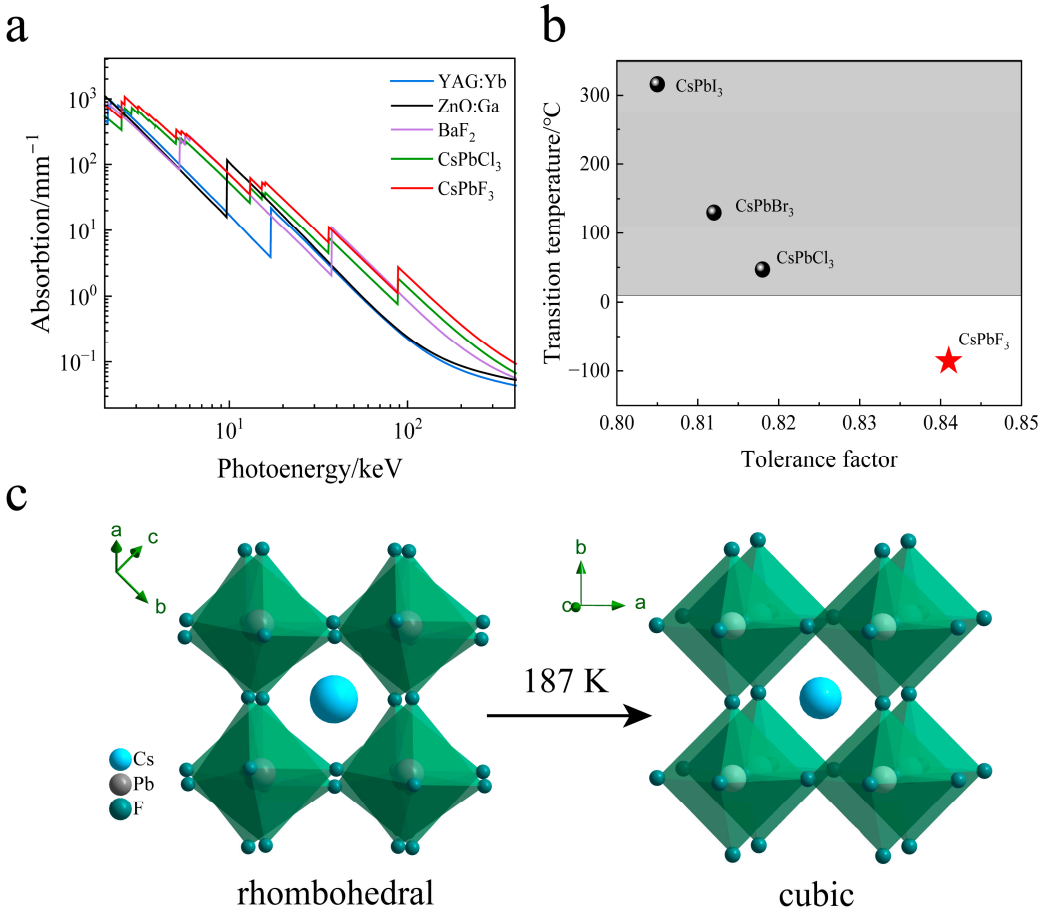

Figure 2. (**a**) Linear attenuation coefficients as a function of photon energy for several fast scintillation crystals. (**b**) The relationship between cubic transition temperature and Goldschmidt tolerance factor. (**c**) A transition of $CsPbF_3$ from a rhombohedral distorted perovskite structure to a cubic perovskite structure at 187 K.

One of the key aspects is the stability of perovskite materials, which can affect the crystal structure transition, has not received sufficient attention. ABX_3-type perovskites can form different crystal structures based on the sizes of the A, B, and X ions. The first requirement is the octahedral factor, which is calculated below:

$$\mu = \frac{r_B}{r_X} \quad (1)$$

where r_B and r_X are the efficient ionic radii of B and X, respectively. The octahedral factor is an important parameter for determining the stability of the ABX_3-type perovskite structure. When the octahedral factor falls in the range of 0.4420–0.8950, the octahedral structure can remain relatively stable. The octahedral factor of $CsPbF_3$ is 0.8947, which is close to the edge of the stable region. The most commonly used and most successful geometric ratio is the Goldschmidt tolerance factor (t_G) [22,23], which can be expressed as follows:

$$t_G = \frac{r_A + r_X}{\sqrt{2}(r_B + r_X)} \quad (2)$$

where r_A is the efficient ionic radii of A. The Goldschmidt tolerance factor is widely used to investigate distorted perovskites. A sTable 3D perovskite phase with high absorption coefficients can be formed within the range of 0.8–1.0. $CsPbF_3$ has a tolerance factor of 0.841, which is close to the edge of the stable perovskite structure. This indicates that $CsPbF_3$ may display unique properties because of its borderline stability.

Figure 2b illustrates the relationship between cubic transition temperature and Goldschmidt tolerance factor of $CsPbX_3$ (X = F^-, Cl^-, Br^-, and I^-) crystals. $CsPbI_3$ tends to crystalize into a yellow non-perovskite phase, which has poor optoelectronic properties at room temperature [24]. There are cubic phase transitions as $CsPbCl_3$ and $CsPbBr_3$ are cooled from high temperature to room temperature. The Bridgman method used to grow these crystals can result in residual stress, twinning, and cracking, which can reduce the yield of high-quality single crystals. Although Zhao et al. managed to find some good quality $CsPbBr_3$ crystals that exhibit an energy resolution of 5.5%, the yield of high-quality single crystals was extremely low (less than 5%) [25]. However, $CsPbF_3$ is in a cubic phase at room temperature, and its phase transition temperature is as low as 187 K. There is no cubic phase transition-induced defects as the crystal grows by the melting method. Due to the strong polar molecular bond of Cs^+ and F^-, $CsPbF_3$ is susceptible to being hygroscopic, and it is prone to oxidation and volatilization at high temperatures. Therefore, obtaining high-quality $CsPbF_3$ crystals can be a challenging task. As shown in Figure 2c, the cubic $CsPbF_3$ is formed by the lead cation and six fluorine ions surrounding the lead cation to form an octahedral coordination. The lead cation locates at the center of the fluorine octahedron; the caesium cation is in the cavity created by the octahedron. At around 187 K, there is the phase transition of $CsPbF_3$ from the rhombohedral distorted perovskite structure to the cubic phase.

The differential thermal analysis (DTA) and thermogravimetric analysis (TG) curves of the perovskite powder are shown in Figure 3a. The DTA heating curve (black line) shows an evident endothermic peak at 629 °C; it is the absorption peak temperature that corresponds to the melting point of $CsPbF_3$. The TG curve indicates that the crystal melts at 629 °C and experiences a steep weight loss, which suggests strong volatility at high temperatures. When using the Bridgman method to prepare crystals, the furnace temperature must be carefully controlled based on the melting point of the crystal. The furnace temperature should be set above the melting point but not excessively high when preparing crystals using the Bridgman method. This is because excessively high temperatures can cause the volatilization of raw materials and lead to component segregation during the crystal preparation process. Hence, the furnace temperature is typically maintained at approximately 660 °C. Figure 3b displays a high-quality $CsPbF_3$ single crystal, which has been polished to a transparent finish with a thickness of 3 mm. The optical clarity of the crystal is apparent, as it is colorless and devoid of any visible macroscopic defects.

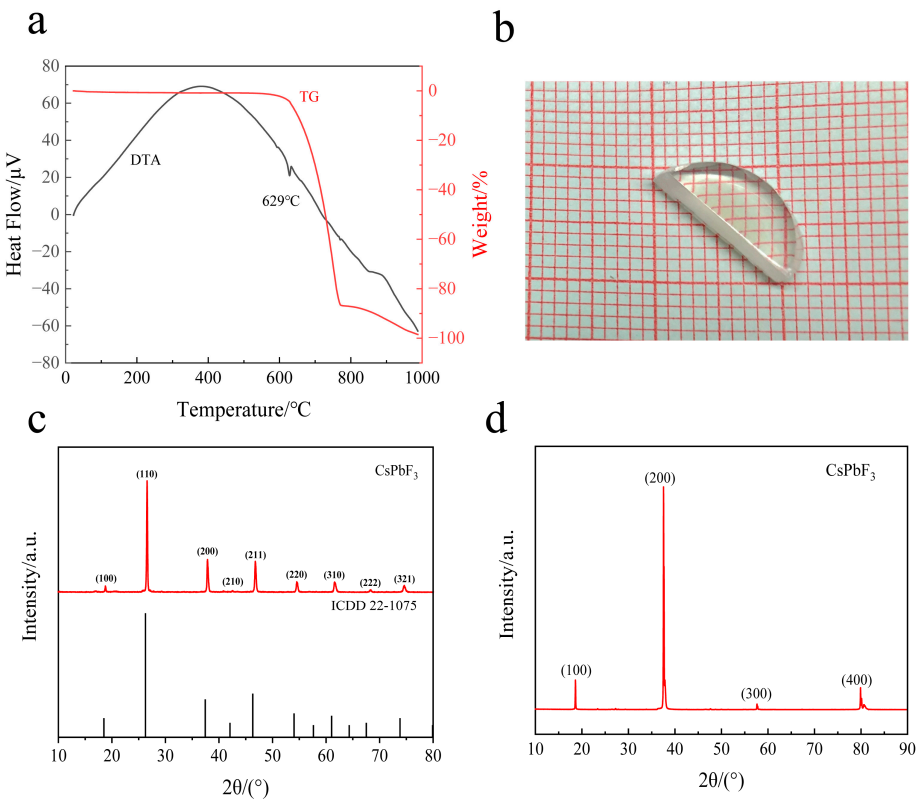

Figure 3. (**a**) DTA (black line) and TG curves (red line) of the $CsPbF_3$ crystal. (**b**) Photograph of $CsPbF_3$ single crystal. (**c**) Powder XRD pattern of the $CsPbF_3$ crystal and standard PDF card (ICDD 22-1075) of the $CsPbF_3$ crystal. (**d**) Cleavage surface XRD pattern of the $CsPbF_3$ crystal.

In Figure 3c, a comparison is presented between the XRD pattern of $CsPbF_3$ and the standard PDF card (ICDD 22-1075) for $CsPbF_3$. The analysis indicates that $CsPbF_3$ has a cubic perovskite structure at room temperature. Additionally, when the crystal boule experiences an impact force, a smooth cleavage surface becomes visible. To investigate this further, cleavage surface XRD pattern analyses were conducted on the surface, and the results are displayed in Figure 3d. The results demonstrate that the (100) surfaces of the $CsPbF_3$ single crystal can be easily cleaved, similar to those of $CsPbCl_3$ [26].

3.2. Optical Properties

The $CsPbF_3$ crystal is known to be hygroscopic in air. In Figure 4a, the mass variation of the crystal as a function of time is presented. During the experiment, the $CsPbF_3$ crystal was exposed to air for 30 h, and its mass increased by 0.8% as a result of its hygroscopic nature. This result highlights the high sensitivity of the crystal to hygroscopicity, emphasizing the importance of encapsulating crystals for any application. To prevent hygroscopicity, the crystals were encapsulated in a quartz box that was filled with nitrogen. Silicone oil coupling was utilized between the quartz windows and the crystal to enhance light collection. Encapsulation has been shown to be an effective method for preventing hygroscopicity, and this packaging technique is both straightforward and efficient.

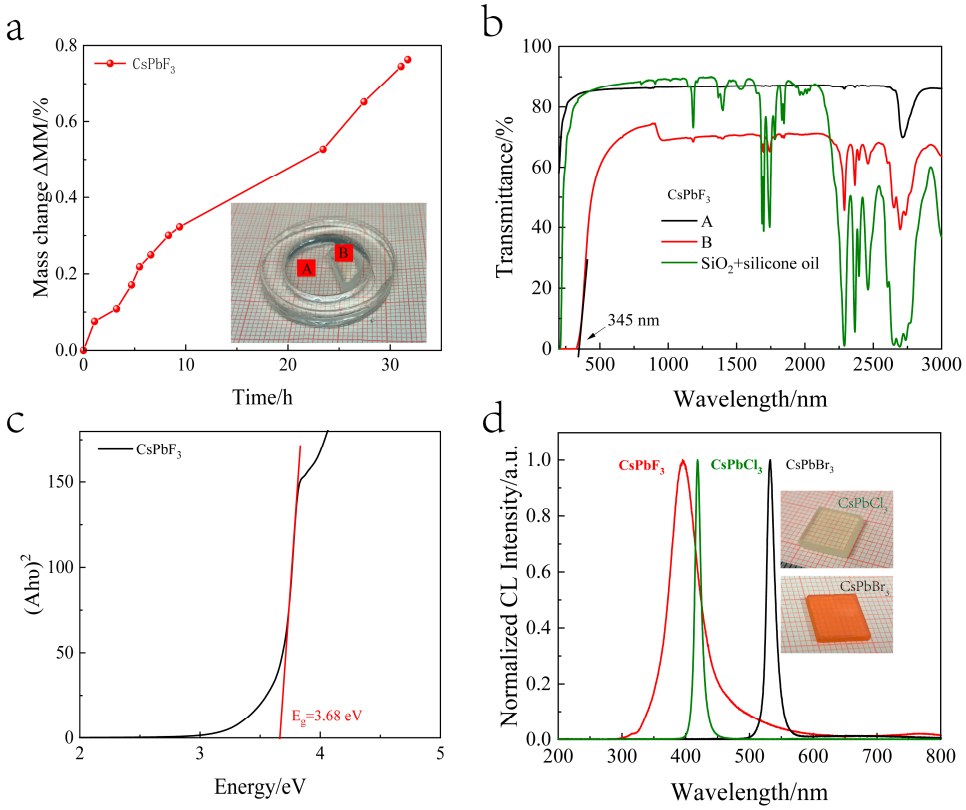

Figure 4. (**a**) The weight of the crystal changes with time. (**b**) Optical transmission spectrum of the $CsPbF_3$ crystal. (**c**) The band gap of the sample was calculated by the Tauc Plot method. (**d**) Cathodoluminescence spectrum of the $CsPbX_3$ (X = F^-, Cl^- and Br^-) crystals.

In order to characterize the optical quality of the single crystal, the transmission spectrum from 200 to 3000 nm is shown in Figure 4b. The black curve corresponds to the A region in Figure 4a, which is equivalent to the cavity between two quartz windows. This structure forms a Fabry–Perot resonator with a lower transmission spectrum compared to the quartz plates. The absorption peak at around 2730 nm is related to OH^-. The transmission spectrum of the A region is also used as a background to analyze the transmission spectrum of the encapsulated crystal. The red curve corresponds to the B region in Figure 4a, which is the transmission spectrum of the encapsulated $CsPbF_3$ sample. The jump of transmittance at 800 nm is attributed to the detector shift of the spectrometer. The transmittance of $CsPbF_3$ is more than 70% from 800 to 3000 nm, and the absorption edge is around 345 nm. The infrared absorption peak in zone B corresponds to the transmission spectrum of the quartz windows and silicone oil (blue line). Meanwhile, the Tauc Plot method was used to calculate the optical bandgap, as shown in Figure 4c. The bandgap of the $CsPbF_3$ crystal is about 3.68 eV, indicating it is a wide bandgap semiconductor. This result is consistent with the calculation results reported [13].

Figure 4d shows CL spectra of $CsPbX_3$ (X = F^-, Cl^-, and Br^-) crystals grown by the Bridgman method. The pictures of $CsPbCl_3$ and $CsPbBr_3$ are also shown in the plot. $CsPbCl_3$ is a light-yellow transparent crystal, and $CsPbBr_3$ is an orange transparent crystal. The CL spectra show the emission wavelengths of $CsPbF_3$, $CsPbCl_3$, and $CsPbBr_3$ are 400 nm, 419 nm, and 534 nm, respectively. They correspond to their direct radiative transitions between the conduction band and valence band. Meanwhile, it demonstrates that the regulation of anions can achieve tunability of the emission wavelength. The full width at half maximum (FWHM) of emission peaks obtained from Gaussian fitting are 54 nm, 12 nm, and 14 nm, respectively. The FWHM value of the $CsPbF_3$ emission peak is larger than that of $CsPbCl_3$ and $CsPbBr_3$, which may be due to spectral broadening induced by crystal surface deterioration.

Figure 5a shows the fluorescence excitation and emission spectra of the $CsPbF_3$ crystal. The excitation wavelength is 208 nm, and the emission peak is around 400 nm, which is consistent with the CL spectrum. Figure 5b displays the fluorescence decay curve of the emission spectrum of $CsPbF_3$ using an excitation wavelength of 300 nm and a monitoring wavelength of 400 nm. The green curve represents the fluorescence decay kinetic curve, and the black line represents the instrument response coefficient. The instrument response coefficient is subtracted by the inverse convolution function. The fitting results indicate that there are three decay components with decay times of 0.4 ns, 2.4 ns, and 15.0 ns, accounting for 30.4%, 50.9%, and 18.7%, respectively. This suggests that the fluorescence luminescence of $CsPbF_3$ is fast. Compared to thin films, perovskite single crystals exhibit a stronger self-absorption effect due to the longer optical path photons take within the crystal, which increases the probability of non-radiative transitions. In the previous works, it was also observed that the PL lifetime of $CsPbBr_3$ single crystals was shorter than that of thin film samples [27,28].

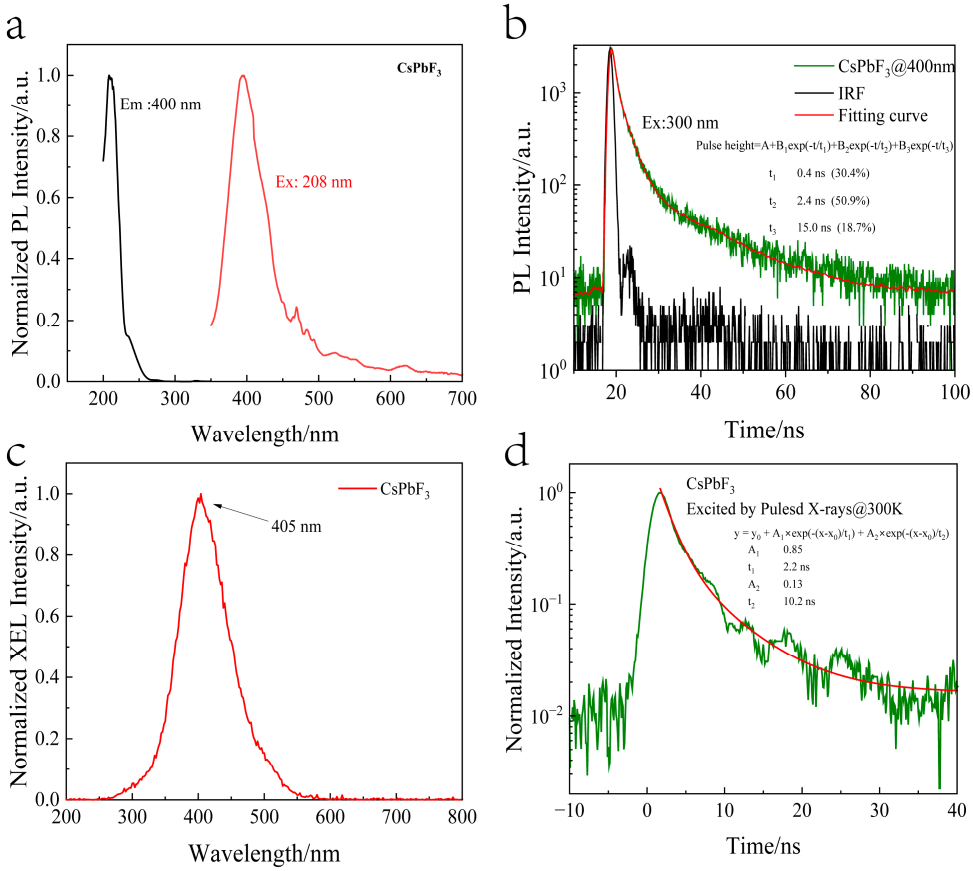

Figure 5. (**a**) Photoluminescence excitation and emission spectra of $CsPbF_3$ crystal. (**b**) Photoluminescence decay curve of $CsPbF_3$ crystal (Excitation: 300 nm; Emission: 400 nm). (**c**) X-ray emission spectra of $CsPbF_3$ crystal. (**d**) Decay kinetics curve excited by the pulsed X-ray.

Figure 5c,d show the X-ray excited luminescence properties of the $CsPbF_3$ crystal. In Figure 5c, the crystal emits light with a slightly redshifted wavelength of 405 nm under X-ray excitation, which is attributed to the self-absorption effect. In Figure 5d, the decay kinetic curve of $CsPbF_3$ crystal excited by the pulsed X-ray is presented. The fitting results indicate that there are two decay components with decay times of 2.2 ns and 10.2 ns. These decay components have a good correspondence with the fluorescence decay components and indicate the potential of $CsPbF_3$ in scintillation luminescent materials.

3.3. Electrical Properties

Figure 6a shows the Current-Voltage (I-V) curve of an ohmic type Au/$CsPbF_3$/Au device, where the thickness of the crystal is 2 mm. The I-V curve provides valuable information on the electrical behaviors of the material, as it shows the relationship between the current flowing through the device and the voltage applied to it. In this case, the resistance of the sample is found to be approximately 2×10^5 Ω, which can be inferred from the slope of the I-V curve at different voltage points. Interestingly, the cyclic I-V curve reveals that the forward scanning curve does not coincide with the reverse scanning curve. This hysteresis effect suggests that the electrical response of the material is not reversible and may be influenced by various mechanisms such as ferroelectric properties, ion vacancy migration, and so on. Although the cubic $CsPbF_3$ does not exhibit ferroelectricity, the hysteresis effect observed in the I-V curve is believed to be related to ion migration, which may be influenced by factors such as defects, impurities, and other material parameters.

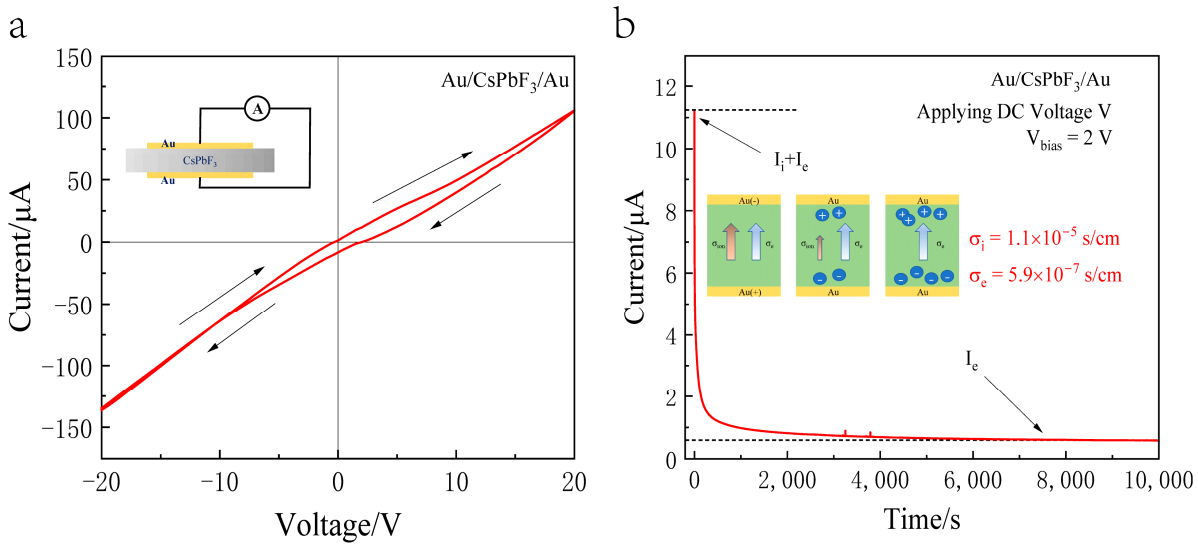

Figure 6. (**a**) Current-Voltage and (**b**) Current-Time characteristic curves of an ohmic type Au/$CsPbF_3$/Au device.

Figure 6b depicts the Current-Time (I-T) curve of the $CsPbF_3$ single crystal under a bias voltage of 2 V, which was employed to determine the ionic and electron conductivities using the DC voltage method. The I-T curve can be separated into three stages, which are dominated by ionic migration, dominated by electron migration, and solely electron migration. The calculated ion conductivity and electron conductivity are 1.1×10^{-5} s/cm and 5.86×10^{-7} s/cm, respectively, indicating that the I-V curve hysteresis effect is linked to fluoride ion migration. The phenomenon of fluoride ion migration is commonly observed in other fluoride materials, including PbF_2, SrF_2, BaF_2, and $PbSnF_4$, which are all considered fluoride ion conductors. Fast ion conductors have also been discovered in gas detectors and solid electrolyte batteries. $CsPbF_3$ is a fast ionic conductor, and its perovskite structure's tolerance factor is located at the boundary of a stable structure. Due to the small ion radius of fluoride ions, they can move freely within the perovskite skeleton created by Pb^{2+}, resulting in fluoride ion migration. $CsPbCl_3$ and $CsPbBr_3$ also exhibit ion migration, which has been exploited in research fields such as photon artificial synapses and memristors [29,30].

The intrinsic instability of perovskite materials towards water, oxygen, and temperature is primarily accountable for their inferior stability. Therefore, before characterizing the electrical performance of the $CsPbF_3$ device, a packaging process was employed, in which the crystal was enclosed with resin casting. The devices that were not electrically tested exhibited insignificant changes in their crystal structure for a duration of one month. Conversely, the electrodes of devices that were exposed to the bias experienced marked

blackening owing to direct contact with the perovskite layer. The exposure of the device to a high-voltage environment instigated electrode decomposition, and the corrosion of the gold electrode by the migration of perovskite ions resulted in apparent discoloration. Hence, the investigation of $CsPbF_3$ stability is an essential research field.

4. Conclusions

This investigation reports the preparation of $CsPbF_3$ single crystal by the Bridgman method. The optical and electrical properties of the synthesized crystal were characterized. The crystal was found to have a band gap of 3.68 eV, a PL emission wavelength of approximately 400 nm, and a fluorescence lifetime with three components: 0.4 ns, 2.4 ns, and 15.0 ns. It was also observed that the $CsPbF_3$ single crystal had a high density and excellent photon cut-off ability. Under pulsed X-ray excitation, the decay times were measured to be 2.2 ns and 10.2 ns, indicating its potential as an ultrafast scintillation crystal. However, it was also noted that $CsPbF_3$ is prone to being hygroscopic and exhibits high ion mobility. These properties make $CsPbF_3$ single crystals promising candidates for various applications, such as ultrafast scintillation materials or visible-blind photoelectric detection devices and more.

Author Contributions: X.Y. and F.Y. conceived the idea and designed the experiments. X.Y., C.G., K.D. and S.L. participated in the crystal growth and preparation. X.Y., C.P., X.H., H.H. and Z.S. performed the device characterization and simulation. B.X., Y.J., R.W., K.Z., Y.L. and W.D. analyzed the data and contributed to the mechanism investigation. X.Y. and F.Y. wrote the manuscript. All authors participated in the discussion and commented on the manuscript. All authors have read and agreed to the published version of the manuscript.

Funding: This research was funded by the National Key R&D Program of China, grant number 2022YFB3503901, the National Natural Science Foundation of China under Grant 12175110, 11775120, 11535010, and Foundation of State Key Laboratory of Intense Pulsed Radiation Simulation and Effect under Grant SKLIPR1805.

Conflicts of Interest: The authors declare no conflict of interest. The funders had no role in the design of the study; in the collection, analyses, or interpretation of data; in the writing of the manuscript; or in the decision to publish the results.

References

1. Liu, X.; Li, J.; Wang, X.; Yang, D. Inorganic lead-based halide perovskites: From fundamental properties to photovoltaic applications. *Mater. Today* **2022**, *61*, 191–217. [CrossRef]
2. Chen, Y.; Feng, Z.; Pal, A.; Zhang, J. Recent Progress on the Performance of Lead-Based Halide Perovskite $APbX_3$ Detectors. *Phys. Status Solidi A* **2022**, *219*, 2200018. [CrossRef]
3. Xu, J.; Maxwell, A.; Wei, M.; Wang, Z.; Chen, B.; Zhu, T.; Sargent, E.H. Defect Tolerance of Mixed B-Site Organic-Inorganic Halide Perovskites. *ACS Energy Lett.* **2021**, *6*, 4220–4227. [CrossRef]
4. Worku, M.; Ben-Akacha, A.; Blessed Shonde, T.; Liu, H.; Ma, B. The Past, Present, and Future of Metal Halide Perovskite Light-Emitting Diodes. *Small* **2021**, *1*, 2000072. [CrossRef]
5. Tian, J.; Xue, Q.; Yao, Q.; Li, N.; Brabec, C.J.; Yip, H.L. Inorganic Halide Perovskite Solar Cells: Progress and Challenges. *Adv. Energy Mater.* **2020**, *10*, 2000183. [CrossRef]
6. Tao, S.; Schmidt, I.; Brocks, G.; Jiang, J.; Tranca, I.; Meerholz, K.; Olthof, S. Absolute energy level positions in tin- and lead-based halide perovskites. *Nat. Commun.* **2019**, *10*, 2560. [CrossRef]
7. He, Y.; Hadar, I.; Kanatzidis, M.G. Detecting ionizing radiation using halide perovskite semiconductors processed through solution and alternative methods. *Nat. Photonics* **2021**, *16*, 14–26. [CrossRef]
8. Ahmad, W.; Khan, J.; Niu, G.; Tang, J. Inorganic $CsPbI_3$ Perovskite-Based Solar Cells: A Choice for a Tandem Device. *Solar RRL* **2017**, *1*, 1700048. [CrossRef]
9. Tan, S.; Yu, B.; Cui, Y.; Meng, F.; Huang, C.; Li, Y.; Chen, Z.; Wu, H.; Shi, J.; Luo, Y.; et al. Temperature-Reliable Low-Dimensional Perovskites Passivated Black-Phase $CsPbI_3$ toward Stable and Efficient Photovoltaics. *Angew. Chem. Int. Ed. Engl.* **2022**, *61*, e202201300. [CrossRef]
10. Yuan, S.; Wang, Z.K.; Zhuo, M.P.; Tian, Q.S.; Jin, Y.; Liao, L.S. Self-Assembled High Quality $CsPbBr_3$ Quantum Dot Films toward Highly Efficient Light-Emitting Diodes. *ACS Nano* **2018**, *12*, 9541–9548. [CrossRef]
11. He, Y.; Petryk, M.; Liu, Z.; Chica, D.G.; Hadar, I.; Leak, C.; Ke, W.; Spanopoulos, I.; Lin, W.; Chung, D.Y.; et al. $CsPbBr_3$ perovskite detectors with 1.4% energy resolution for high-energy γ-rays. *Nat. Photonics* **2020**, *15*, 36–42. [CrossRef]

12. He, Y.; Stoumpos, C.C.; Hadar, I.; Luo, Z.; McCall, K.M.; Liu, Z.; Chung, D.Y.; Wessels, B.W.; Kanatzidis, M.G. Demonstration of Energy-Resolved gamma-Ray Detection at Room Temperature by the $CsPbCl_3$ Perovskite Semiconductor. *J. Am. Chem. Soc.* **2021**, *143*, 2068–2077. [CrossRef] [PubMed]
13. Mykhaylyk, V.B.; Rudko, M.; Kraus, H.; Kapustianyk, V.; Kolomiets, V.; Vitoratou, N.; Chornodolskyy, Y.; Voloshinovskii, A.S.; Vasylechko, L. Ultra-fast low temperature scintillation and X-ray luminescence of $CsPbCl_3$ crystals. *J. Mater. Chem. C* **2023**, *11*, 656–665. [CrossRef]
14. Murtaza, G.; Ahmad, I.; Maqbool, M.; Aliabad, H.A.R.; Afaq, A. Structural and Optoelectronic Properties of Cubic $CsPbF_3$ for Novel Applications. *Chinese Phys. Lett.* **2011**, *28*, 117803. [CrossRef]
15. Bouznik, V.M.; Moskvich, Y.N.; Voronov, V.N. Nuclear magnetic resonance study of ^{19}F motion in $CsPbF_3$. *Chem. Phys. Lett.* **1976**, *37*, 464–467. [CrossRef]
16. Berastegui, P.; Hull, S.; Eriksson, S.-G. A low-temperature structural phase transition in $CsPbF_3$. *J. Phys. Condens. Matter.* **2001**, *13*, 5077–5088. [CrossRef]
17. Smith, E.H.; Benedek, N.A.; Fennie, C.J. Interplay of Octahedral Rotations and Lone Pair Ferroelectricity in $CsPbF_3$. *Inorg. Chem.* **2015**, *54*, 8536–8543. [CrossRef]
18. Wang, J.; Hao, J.; Duan, C.; Wang, X.; Wang, K.; Ma, C. A Fluoride-Ion-Conducting Solid Electrolyte with Both High Conductivity and Excellent Electrochemical Stability. *Small* **2022**, *18*, e2104508. [CrossRef]
19. Song, J.; Cui, Q.; Li, J.; Xu, J.; Wang, Y.; Xu, L.; Xue, J.; Dong, Y.; Tian, T.; Sun, H.; et al. Ultralarge All-Inorganic Perovskite Bulk Single Crystal for High-Performance Visible-Infrared Dual-Modal Photodetectors. *Adv. Opt. Mater.* **2017**, *5*, 1700157. [CrossRef]
20. Vanecek, V.; Kral, R.; Paterek, J.; Babin, V.; Jary, V.; Hybler, J.; Kodama, S.; Kurosawa, S.; Yokota, Y.; Yoshikawa, A.; et al. Modified vertical Bridgman method: Time and cost effective tool for preparation of Cs_2HfCl_6 single crystals. *J. Cryst. Growth* **2020**, *533*, 125479. [CrossRef]
21. Zhang, P.; Zhang, G.; Liu, L.; Ju, D.; Zhang, L.; Cheng, K.; Tao, X. Anisotropic Optoelectronic Properties of Melt-Grown Bulk $CsPbBr_3$ Single Crystal. *J. Phys. Chem. Lett.* **2018**, *9*, 5040–5046. [CrossRef] [PubMed]
22. Charles, B.; Dillon, J.; Weber, O.J.; Islam, M.S.; Weller, M.T. Understanding the stability of mixed A-cation lead iodide perovskites. *J. Mater. Chem. A* **2017**, *5*, 22495–22499. [CrossRef]
23. Li, Z.; Yang, M.; Park, J.S.; Wei, S.H.; Berry, J.J.; Zhu, K. Stabilizing Perovskite Structures by Tuning Tolerance Factor: Formation of Formamidinium and Cesium Lead Iodide Solid-State Alloys. *Chem. Mater.* **2015**, *28*, 284–292. [CrossRef]
24. Straus, D.B.; Guo, S.; Cava, R.J. Kinetically Stable Single Crystals of Perovskite-Phase $CsPbI_3$. *J. Am. Chem. Soc.* **2019**, *141*, 11435–11439. [CrossRef] [PubMed]
25. Zhao, L.; Zhou, Y.; Shi, Z.; Ni, Z.; Wang, M.; Liu, Y.; Huang, J. High-yield growth of $FACsPbBr_3$ single crystals with low defect density from mixed solvents for gamma-ray spectroscopy. *Nat. Photonics.* **2023**, *17*, 315–323. [CrossRef]
26. Kobayashi, M.; Omata, K.; Sugimoto, S.; Tamagawa, Y.; Kuroiwa, T.; Asada, H.; Takeuchi, H.; Kondo, S. Scintillation characteristics of $CsPbCl_3$ single crystals. *Nucl. Instrum. Methods. Phys. Res. B* **2008**, *592*, 369–373. [CrossRef]
27. Li, C.; Zang, Z.; Han, C.; Hu, Z.; Tang, X.; Du, J.; Leng, Y.; Sun, K. Highly compact $CsPbBr_3$ perovskite thin films decorated by ZnO nanoparticles for enhanced random lasing. *Nano Energy* **2017**, *40*, 195–202. [CrossRef]
28. Pan, L.; Pandey, I.R.; Miceli, A.; Klepov, V.V.; Chung, D.Y.; Kanatzidis, M.G. Perovskite $CsPbBr_3$ Single-Crystal Detector Operating at 10^{10} Photons s^{-1} mm^{-2} for Ultra-High Flux X-ray Detection. *Adv. Opt. Mater.* **2023**, *11*, 2202946. [CrossRef]
29. Yang, L.; Singh, M.; Shen, S.W.; Chih, K.Y.; Liu, S.W.; Wu, C.I.; Chu, C.W.; Lin, H.W. Transparent and Flexible Inorganic Perovskite Photonic Artificial Synapses with Dual-Mode Operation. *Adv. Funct. Mater.* **2020**, *31*, 2008259. [CrossRef]
30. Wu, Y.; Wei, Y.; Huang, Y.; Cao, F.; Yu, D.; Li, X.; Zeng, H. Capping $CsPbBr_3$ with ZnO to improve performance and stability of perovskite memristors. *Nano Res.* **2016**, *10*, 1584–1594. [CrossRef]

Disclaimer/Publisher's Note: The statements, opinions and data contained in all publications are solely those of the individual author(s) and contributor(s) and not of MDPI and/or the editor(s). MDPI and/or the editor(s) disclaim responsibility for any injury to people or property resulting from any ideas, methods, instructions or products referred to in the content.